Ceiling Effects for Hybrid Aerial–Surface Locomotion of Small Rotorcraft

Yi Hsuan Hsiao and Pakpong Chirarattananon , *Member, IEEE*

Abstract—As platform size is reduced, the flight of aerial robots becomes increasingly energetically expensive. Limitations on payload and endurance of these small robots have prompted researchers to explore the use of bimodal aerial–surface locomotion as a strategy to prolong operation time while retaining a high vantage point. In this paper, we propose the use of "ceiling effects" as a power conserving strategy for small rotorcraft to perch on an overhang. In the vicinity of a ceiling, spinning propellers generate markedly higher thrust. To understand the observed aerodynamic phenomena, momentum theory and blade element method are employed to describe the thrust, power, and rotational rate of spinning propellers in terms of propeller-to-ceiling distance. The models, which take into account the influence of neighboring propellers as present in multirotor vehicles, are verified using two propeller types (23-mm and 50-mm radii) in various configurations on a benchtop setup. The results are consistent with the proposed models. In proximity to the ceiling, power consumption of propellers with 23-mm radius arranged in a quadrotor configuration was found to reduce by a factor of three. To this end, we present a conceptual prototype that demonstrates the use of ceiling effects for perching maneuvers. Overall, the promising outcomes highlight possible uses of ceiling effects for efficient bimodal locomotion in small multirotor vehicles.

NOMENCLATURE

R	Propeller's radius.
D	Propeller-to-ceiling distance.
δ	Propeller-to-ceiling ratio (R/D).
v, v_i	Local and induced flow velocities.
p, p_0	Local and atmospheric air pressures.
A	Area of the propeller disc: $A = \pi R^2$.
ρ	Air density.
T	Propelling thrust.
P_a, P_m	Aerodynamic and mechanical powers.
γ	Dimensionless ceiling coefficient.
L	Propeller-to-propeller distance.
α_0, α_1	Dimensionless coefficients describing the nonaxisymmetric flow and wake recirculation.
η	Figure of merit.
Ω	Propeller's angular rate.
c_T, c_τ	Propeller's thrust and torque coefficients.
c_0, c_1, c_2	Dimensionless propeller's blade coefficients.

I. INTRODUCTION

IN THE past decade, we have witnessed growing developments of micro aerial vehicles (MAVs). The rapid advancement of these small flying robots, or drones, is driven by perceivable impacts on a wide range of applications: transportation and delivery of medical supplies, environmental monitoring, or enabling ad-hoc network communication in disaster areas. To date, researchers have demonstrated flight across various robotic platforms ranging from fixed-wing aircraft with wingspans of meters [1], [2], a swarm of centimeter-scale quadrotors [3], [4], to millimeter-scale flapping-wing robots [5], [6]. Among these, multirotor robots have been widely recognized in both research and end-user communities owing to the relative ease of use and expansive functionalities.

However, the high energetic cost of staying airborne poses a major challenge. The flight time of MAVs is severely constrained by the onboard power supplies. Compared to fixed-wing counterparts, rotorcraft encounter an issue of reduction in flight endurance due to the lack of a large aerodynamically efficient planform. At centimeter scales, flight at low Reynolds numbers is increasingly difficult thanks to higher viscous losses [7]. The problem aggravates as the power density of electromagnetic motors decreases and friction becomes dominant. Flight time of sub-kilogram rotary vehicles swiftly diminishes to minutes [8]. This energetic limitation hinders small flying robots from completing an extended operation or accomplishing autonomous capabilities that require substantial payload and power budget for sensors and computation.

Several strategies have been investigated to address the constraints on payload and flight endurance. In order to expand the navigation abilities of small robots with limited sensing and computational power, bio-inspired approaches, such as optic flow-based strategies, have been explored to enable MAVs to reactively navigate and avoid collisions [9], [10]. Control and planning methods for efficient rotorcraft flight have been

proposed [11], [12]. Alternatively, to workaround the elevated costs of aerial transport, researchers have also demonstrated usages of multimodal locomotion [13], equipping flying robots with abilities to traverse over terrain [14], or perform underwater maneuvers [6], [15], [16]. Hybrid aerial and surface locomotion has emerged as another solution that allows flying robots to perch on surfaces to conserve power while continuing to carry on functional assignments, such as monitoring, inspection, or communication [17]. To attach to vertical surfaces or overhangs, various mechanical attachment techniques and adhesions have been proposed [5], [17]–[21]. Common solutions exploit microspines, adhesives, or grasping mechanisms designed for repeatable attachment and detachment.

This paper investigates the use of ceiling effects for small rotorcraft to perch on an overhang. With the presence of a ceiling above a spinning propeller, the structure disrupts the upstream wake. The airflow in the limited volume between the ceiling and the propeller lowers the local pressure, effectively attracting the propeller toward the surface. As a result, the spinning propeller experiences a substantial increase in aerodynamic force. The additional thrust potentially allows a robot to stay aloft at a high vantage point while consuming less energy. The use of such effects would conceivably enhance operations of small rotary-wing vehicles in indoor settings or urban environments with high-rises and elevated structures.

Until now, aerodynamic studies of proximity effects on spinning propellers are predominantly limited to investigations of ground effects on helicopters. Based on models using the method of images and a surface singularity, and experimental validation [22]–[25], the ground effect was found to decrease power consumption by up to 50% when the propellers are extremely close to the ground [23]. The effects, however, are negligible when the propeller is more than one diameter above the ground. Small multirotors typically possess relatively small propellers with an airframe situated below the propellers. This inevitably enlarges the gap between the ground and the rotors, rendering the ground effects insignificant [26]. In contrast, we foresee that small MAVs have potential to benefit from the ceiling effects when operating indoors or under structural overhangs as the separation between the ceiling and the propellers can be minimized. Apart from the preliminary findings in [27], to date, little has been researched on the topic of ceiling effects as they are irrelevant to flight of traditional helicopters. In the context of MAVs, a brief study of the ceiling effects was provided in [26], citing that the resultant force attracts the vehicle toward the ceiling, increasing the chances of an undesirable collision.

This work entails the systematic study of the ceiling effects for small rotorcraft in terms of force and power. Potential uses of such effects include the hybrid aerial–surface locomotion for power conservation. Initially, the impact of a horizontal surface in proximity to a rotor is analyzed based on classical momentum theory (MT) to yield the connection between aerodynamic power and thrust. Despite requiring some assumptions on the flow conditions, MT is often employed to describe airflow through wind turbines and propellers [22], [24], [28]–[31]. As first presented in [27], MT provides insights into the relationship between the generated thrust and the aerodynamic power as a function of the propeller-to-ceiling distance. It turns out that the reduction in aerodynamic power due to the presence of a ceiling can be quantified using the introduced parameter—ceiling coefficient.

Unlike a single propeller, there might exist flow interaction between multiple propellers on multirotor robots, we propose that the values of the ceiling coefficient are also affected by nearby propellers for the case of multirotor systems owing to asymmetry and flow recirculation. Next, to gain better insights into how the ceiling affects the performance of MAVs in flight, the blade element method (BEM) is incorporated to relate the thrust and power to the rotational rate of the blade to obtain the thrust and torque coefficients of the propellers. The thrust and torque coefficients—critical numbers for modeling and flight control applications—are no longer constant as in free flight, but dependent on the gap between the ceiling and the propellers.

The proposed models are verified by a series of benchtop experiments on two propeller types in a single and multiple propellers configurations, with thrust, torque, rotational rate, and power consumptions recorded for analysis. This allows direct comparison between the empirically determined ceiling coefficients, and thrust and torque coefficients against the model predictions. Last, discussion on the power saving and practical uses of ceiling effects on a small quadrotor to realize hybrid aerial and surface locomotion is given.

II. MT FOR AXISYMMETRIC FLOW

To quantitatively explain how the presence of a ceiling alters the power consumption of a spinning propeller, in this section, MT is employed to describe the aerodynamic forces and power associated with a single spinning propeller placed below a flat surface. To begin, consider the situation described by the diagram in Fig. 1(a), an infinitely thin spinning propeller with radius R is located at the coordinate $z = -D$ from the horizontal surface at $z = 0$. To apply MT, standard assumptions are used, including that the flow is steady, incompressible, and axisymmetric, the fluid is homogeneous, inviscid, and irrotational, and the propeller produces thrust by applying the load uniformly through the actuator disc. Similar to other models that describe rotors or wind turbines [29]–[31], the flow immediately above and underneath the propeller is assumed to be one-dimensional (1-D). That is, for a stationary propeller, such as that of a quadrotor in hover, the rotating propeller induces the uniform vertical airflow, v_i. This induced velocity is continuous above and below the propeller disc, consistent with the continuity condition. However, the actuator disc creates an abrupt change in pressure [from p_- to p_+ as illustrated in Fig. 1(a)]. The difference between the downstream and upstream pressures results in the thrust $T = (p_+ - p_-) A$. The aerodynamic power is given by $P_a = T v_i$.

The presence of the ceiling affects the airflow above the propeller as it prevents the upstream air from entering the propeller directly. When employing the inviscid flow assumption, we drop the no-slip condition at the wall. It follows that the flow adjacent to the ceiling above the propeller is radially inward. For a small gap D, it is reasonable to assume that the incoming air at $r = R$
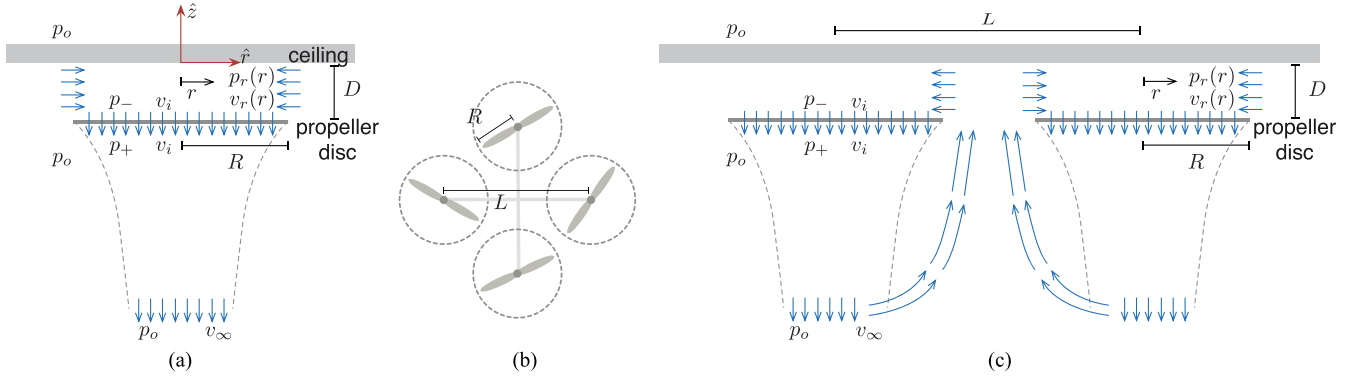
Fig. 1.   Spinning propeller is treated as a thin circular disc situated at the distance D below the ceiling. The axisymmetric cylindrical coordinate frame is placed along the axis of the rotor. The diagram defines the pressure and flow speed at different parts of the system.

travels horizontally. The radial component of the flow above the propeller (v_r) is assumed to be only dependent on r, independent of the distance from the ceiling. To relate v_r to the induced velocity v_i, apply the fact that the airflow radially entering an imaginary cylinder of radius r must vertically exit the cylinder through the propeller below: $2\pi r D \cdot v_r\left(r\right) = \pi r^2 v_i$, or

$$v_r\left(r\right) = \frac{r}{2D}v_i \quad \text{for } r \in [0, R].$$ (1)

The Bernoulli equation characterizes the relationship between pressure and velocity of the wake along a streamline [24]. The upstream air pressures at the ceiling (p_r) and above the propeller disc satisfy

$$p_0 = p_r\left(r\right) + \frac{1}{2}\rho v_r^2\left(r\right) = p_- + \frac{1}{2}\rho v_i^2.$$ (2)

Whereas the downstream pressure is related to the terminal flow velocity such that $p_+ + \frac{1}{2}\rho v_i^2 = p_o + \frac{1}{2}\rho v_\infty^2$.

In regular circumstances, MT states that the thrust force T is equal to the difference between the vertical momentum of the incoming and outgoing airflow. In this case, the presence of the ceiling must be taken into account. Consider an imaginary cylinder of radius R with the top region above the ceiling and the bottom cap infinitely far away, where the wake has reached terminal velocity, and apply the conservation of momentum along the vertical direction to objects and the airflow in this volume. Two external forces include the propelling thrust (T) and the holding force that constrains the ceiling against the pressure difference above and below the ceiling. The thrust can be found as

$$T = \left(p_+ - p_-\right)A = \frac{1}{2}\rho A v_\infty^2.$$ (3)

The magnitude of the holding force ($\Delta p \cdot A$) applied to the ceiling is obtained by integrating $p_r\left(r\right)$ over the surface

$$\Delta p \cdot A = p_o A - \int_{r=0}^{R} p_r(r)2\pi r dr = \frac{1}{16}\rho A v_i^2\left(\frac{R}{D}\right)^2$$ (4)

where $p_r\left(r\right)$ has been substituted by $v_r\left(r\right)$, and then, v_i from (2) and (1). In the meantime, it can be seen that the air enters this imaginary volume horizontally, contributing to zero vertical momentum. The outgoing flow, with the mass rate $\dot{m} = \rho A v_i$,

carries the exit momentum $\dot{m}v_\infty = \rho A v_i v_\infty$. In total, the conservation of momentum yields

$$\frac{1}{2}\rho A v_\infty^2 - \rho A v_i v_\infty - \frac{1}{16}\rho A v_i^2\left(\frac{R}{D}\right)^2 = 0.$$ (5)

The last term in (5) distinguishes the considered situation from the no-ceiling case. That is, the ceiling affects the flow momentum through the pressure difference above and below the surface. This equation has one physically feasible solution

$$v_i = \frac{2}{1 + \sqrt{1 + \frac{1}{8}\delta^2}}\frac{1}{2}v_\infty = \frac{1}{2}\gamma^{-1}v_\infty$$ (6)

where a dimensionless ceiling coefficient $\gamma := \frac{1}{2} + \frac{1}{2}\sqrt{1 + \frac{1}{8}\delta^2}$ and the propeller to ceiling ratio $\delta := R/D$ are introduced to capture the effects of the ceiling. When the ceiling is absent (infinitely far away), $\gamma \to 1$ as found in a regular case [29]. Otherwise, γ is larger than unity and monotonically increases as D decreases.

From here, the aerodynamic power is found from $P_a = Tv_i$ in terms of T and γ using (3) and (6) as

$$P_a = \gamma^{-1}T\sqrt{\frac{T}{2\rho A}}$$ (7)

which implies that, when the ceiling is present ($\gamma > 1$), the propeller requires a factor of γ less power to generate the same thrust. In other words, multirotor vehicles can potentially reduce power consumption by flying near a ceiling or perching on an overhang.

III. EFFICIENCY LOSSES AND MULTIROTOR INTERACTION

Thus far, the proposed models rely on several assumptions, including the absence of viscosity and irrotationality, and the symmetry of the system. It turns out that the simplified model cannot accurately capture the observed results when multiple rotors operate simultaneously in a quadrotor configuration as depicted in Fig. 1(b). This section examines two primary factors related to the symmetry of the system and the interaction between adjacent propellers. These considerations can then be incorporated into the proposed ceiling coefficient.

A. Irrotational Nonaxisymmetric Flow

The use of MT in Section II assumes quasi-steady flow. The assumption on axisymmetry is somewhat equivalent to having an infinite number of infinitesimal blades. This, subsequently, leads to a reasonable time-averaged result. For a more realistic analysis applicable to a system with finite number of blades, the axisymmetric assumption is relaxed. That is, the induced velocity v_i is allowed to be dependent on θ [defined as the angle about the $\hat{z}$ axis in Fig. 1(a)]. Still, the angular component remains zero. By considering only the first-order variation, it is reasonable to assume

$$v_i (\theta, \alpha_0) = v_i \left(1 + \sqrt{2 (\alpha_0 - 1)} \cos \theta \right) \tag{8}$$

where the term $\cos \theta$, without loss of generality, describes the first harmonic variation in θ, and α_0 indicates the magnitude of the angular variation ($\alpha_0 \geq 1$). When $\alpha_0 = 1$, $v_i (\theta, \alpha) = v_i$ is recovered. In this form, the average flow velocity is unchanged.

The conservation of mass, as a consequence, requires the radial velocity of the flow above the propeller to be dependent on θ, changing (1) to $v_r (r, \theta) = \frac{r}{2D} v_i (\theta, \alpha_0)$. This alters the average pressure applied to the ceiling. The new holding force [previously given by (4)] is

$$\Delta p \cdot A = \frac{1}{16} \alpha_0 \rho A v_i^2 \left(\frac{R}{D} \right)^2 . \tag{9}$$

When incorporated into conservation of momentum or (5), the ceiling coefficient becomes $\gamma (\delta, \alpha_0) := \frac{1}{2} + \frac{1}{2} \sqrt{1 + \frac{\alpha_0}{8} \delta^2}$. The angular variation factor, α_0, can be also be regarded as an empirical coefficient that accounts for other simplifying assumptions, such as boundary layer effects, or it can be treated as a factor for adjusting the effective radius of the propeller blade. The inclusion of α_0 does not affect γ when the ceiling is absent or $\delta = 0$.

While in a single propeller case, the time-averaged flow may appear highly symmetrical. It is likely that at shorter timescales, comparable to the rotational velocity of the blades, the wake has some angular variation. This will result in the value of $\alpha_0 > 1$, amplifying the ceiling coefficient and rendering the propeller more efficient near a surface. Moreover, it is perceivable that with multiple rotors operating in proximity, the flow interactions would disrupt the symmetry of the flow around each propeller, boosting the effective value of α_0. These trends are, in fact, observed in the experiments performed in Section V.

B. Tip Loss and Recirculation

With the well-defined streamtube as shown in Fig. 1(a), MT and BEM usually neglect tip loss. In reality, the discontinuity in pressure immediately above and below the propeller disc draws some downstream air to escape outward between the blade tips and re-enter as tip vortices [28]. This essentially reduces the total induced flow and is known as tip loss. In the case of ground effect, it is known that the induced velocity is influenced as the ground prohibits the downward velocity of the wake, resulting in a lower induced velocity for the same thrust [28]. The ground also affects the diffusion of tip vortices [32]. In [33],

PIV experiments show that the presence of the ground causes the recirculation of the wake at a larger scale—the effect also known as *brownout*.

For a spinning propeller underneath a horizontal surface, we hypothesize that part of the wake recirculates in a similar fashion. This phenomenon is likely more pronounced when multiple propellers are present. As illustrated in Fig. 1(c), when propeller discs are placed at distance L from one another, their presence obstructs the air from entering the streamtubes above the propellers. This inevitably leads to recirculation of the wake, resulting in the reduction of the terminal flow momentum. We postulate that, depending on the distance between the propeller to the ceiling, a small portion of the wake (denoted by $\alpha_1 \delta^2$) recirculates. In this form, the recirculation is more pronounced when the propeller is closer to the ceiling. As a result, the terminal vertical flow momentum decreases from $\dot{m} v_\infty$ to $\left(1 - \alpha_1 \delta^2 \right) \dot{m} v_\infty$, whereas the upstream flow and the ceiling pressure are not directly affected. This modifies the previous conservation of momentum (5). If the earlier angular variation factor is also considered, the revised ceiling coefficient becomes

$$\gamma (\delta, \alpha_0, \alpha_1) := \frac{1}{2} \left(1 - \alpha_1 \delta^2 \right) + \frac{1}{2} \sqrt{(1 - \alpha_1 \delta^2)^2 + \frac{\alpha_0}{8} \delta^2}. \tag{10}$$

The recirculation crucially lowers the ceiling coefficient, making the propeller less energetically efficient. This is because the recirculation inherently assumes that the downwash loses its energy before re-entering the upstream wake. In the scenario, where multiple rotors are together, it is anticipated that the neighboring propellers would strengthen the recirculation, resulting in a larger α_1 when the distance between the propellers (L) shrinks. Nevertheless, the recirculation caused by nearby propellers breaks the axisymmetric profile of the wake. This, in turn, increases α_0, rendering the propeller to be more efficient. These two competing phenomena play an important role in the resultant ceiling coefficient when multiple propellers operate in a multirotor vehicle configuration.

In this form, the ceiling coefficient still asymptotically approaches unity as the ceiling is infinitely far away, independent of α_1. In other words, the parameter α_1 captures the interaction between the propellers that are caused by the presence of a ceiling. However, it does not describe the interactions that may already exist without the ceiling.

C. Figure of Merit and Power

At the end of Section II, the relationship between the aerodynamic power (P_a) and thrust has been presented. This represents the power delivered by the spinning propeller to the air. The aerodynamic power, however, is less than the mechanical power delivered by the motor (measurable as the product of torque and angular velocity, $P_m = \tau \Omega$) owing to losses from wake rotation, nonuniform flow, and tip vortices not captured by MT [24], [29]. Figure of merit (η) accounts for the difference, representing the aerodynamic efficiency of the rotor

$$P_a = \eta P_m . \tag{11}$$

This figure of merit is typically lower for smaller rotors as they are inherently less efficient. For simplicity, it is usually assumed constant for a particular propeller, regardless of the rotational rate.

For a motor–propeller system, the input power into the system ($P_i = IV$) is also different from the mechanical power due to heat dissipation and frictional losses. For a brushed motor, we consider the first-order motor model in steady state: $V = IR_i + V_e$, where R_i is the effective motor's internal resistance, and $V_e = k\Omega$ is the back EMF, linearly proportional to Ω. The mechanical power of the motor is often assumed identical to the electrical power subtracted by the resistive loss, $P_m = IV_e = Ik\Omega$. This renders P_m to always be lower than P_i. For a brushless motor driven by a three phase signal generated by an electronic speed controller (ESC), the input voltage is approximately constant while the ESC regulates the current to vary the output power. The mechanical power is equal to the input power subtracted by losses in the internal resistance and the ESC. In such cases, it is more sophisticated to determine the mechanical power from the input voltage and current, however, it can be calculated from the torque and angular velocity measurements.

IV. THRUST AND TORQUE COEFFICIENTS FOR FLIGHT

A. Blade Element MT

Using MT, the relationship between the generated thrust and aerodynamic power is given by (7). The presence of a horizontal surface or ceiling above the propeller modifies this relationship through the ceiling coefficient. MT alone, however, does not relate the aerodynamic power and thrust to the propeller's speed or the torque it experiences. In this section, BEM is used to consider the geometry of the propeller to estimate the thrust, torque, and power when the propeller spins at the angular rate Ω. Incorporating this with the ceiling coefficient, the thrust and torque coefficients of a spinning propeller are evaluated in terms of the ceiling coefficient. These parameters are important for flight in the vicinity of a ceiling as the produced force and torque are affected by the ceiling even when the angular rate is maintained.

Here, readers are referred to [29] and the supplemental materials. In [29], blade element momentum theory (BEMT) was used to derive an equation describing the relationship between thrust, induced velocity, and the angular rate of a propeller. As previously shown in Section II, with the presence of a nearby ceiling, the upstream wake acquires some radial velocity. This is distinct from a regular flight condition, where a rotor only experiences vertical and horizontal flow. As a consequence, the previous result from [29] must be modified to take into account the contribution from radial flow across the propeller blades. As derived in the supplemental materials, the equation for thrust from BEM becomes

$$T = \frac{1}{2}\rho A R^2 \left(c_0 - c_1 \frac{v_i}{\Omega R} + c_2 \frac{v_i}{\Omega R}\delta \right)\Omega^2 \qquad (12)$$

where the coefficients c_0, c_1, and c_2 are related to the blade profile. The last term is dependent on the propeller-to-ceiling ratio,

which asymptotically vanishes when the ceiling is infinitely far away. In this form, the thrust coefficient[1] $c_T := T/\Omega^2$ cannot be immediately derived from (12) owing to the presence of v_i. However, (3) states that $T = \frac{1}{2}\rho A v_\infty^2$. With the definition of the ceiling coefficient, this can be written in terms of the induced velocity v_i as

$$T = 2\rho A \gamma^2 v_i^2. \qquad (13)$$

Equating T from (12) and (13) let us solve for $\Omega R/v_i$. When substituted back to (12), the thrust coefficient is obtained, $c_T := T/\Omega^2$

$$c_T = 2\rho A \left(\frac{2c_0 R\gamma}{(c_1 - c_2\delta) + \sqrt{(c_1 - c_2\delta)^2 + 16c_0\gamma^2}} \right)^2. \qquad (14)$$

The thrust coefficient depends on the ceiling coefficient and δ. Without the ceiling, this coefficient reduces to $c_T|_{\gamma=1} = 8\rho A \left[c_0 R / \left(c_1 + \sqrt{c_1 + 16c_0} \right) \right]^2$.

To evaluate the torque coefficient $c_\tau := \tau/\Omega^2$, we use the fact that $P_m = \tau\Omega = c_\tau\Omega^3$, $P_a = Tv_i$, and $P_a = \eta P_m$. It follows that

$$c_\tau = \frac{1}{\eta\sqrt{2\rho A}} c_T^{3/2}. \qquad (15)$$

Far away from the ceiling $c_\tau|_\gamma = 1 = (16\rho A/\eta)\left[c_0 R/(c_1 + \sqrt{c_1 + 16c_0})\right]^3$. As anticipated, without the ceiling and, hence, radial flow, the parameter c_2 disappears from the expression of thrust and torque coefficients.

V. BENCHTOP EXPERIMENTS

In this section, experiments are conducted to verify the aerodynamic models for two propeller sizes. The experimental procedure is designed such that ceiling and propeller coefficients can be empirically evaluated under various conditions. The results enable the verification of the following.

1) The relationship between power and thrust at various propeller-to-ceiling distances.
2) The impact of multirotor interaction.
3) The resultant thrust and torque coefficients.

A. Experimental Setup

Two motor–propeller combinations were employed for the experiments. Each motor and propeller combination was mounted on a multiaxis force/force sensor (nano17, ATI) via a 3-D printed structure (Black Resin, Formlabs Form 2) as illustrated in Fig. 2. Two 5 mm-thick transparent acrylic plates (with the total thickness of 10 mm) were mounted on a linear motorized positioning stage as a ceiling. The stage was driven by a microstepping driver (M542, Leadshine) for adjusting the distance between the propeller and the ceiling, yielding a step size of 20 μm.

For generation of driving signals and data acquisition, a computer running the Simulink Real-Time (Mathworks) system

---

[1]The thrust and torque coefficients (c_T and c_τ) are defined as commonly used in analysis of aerial vehicles [29], slightly different from the dimensionless definitions used in aerodynamics research.
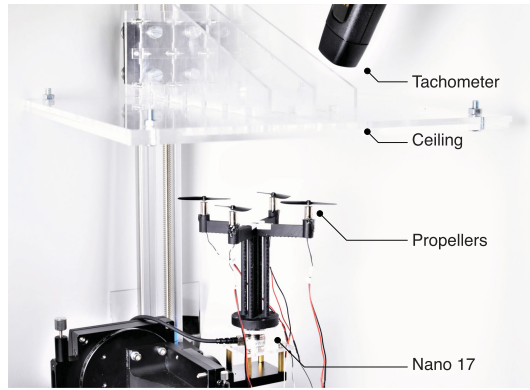
Fig. 2. Photo depicting the experimental setup with four 23-mm propellers mounted on a force/torque sensor. The ceiling, which translates vertically, is controlled by a motorized stage. The tachometer placed above the ceiling measures the rotational rate belonging to one of the propellers.

with a DAQ (PCI-6229, National Instruments) was used for generating command signals for driving the motor and the ceiling, recording force/torque measurements, and collecting voltage and current data. The Advent Optical A2108 tachometer with an analog output was installed above the transparent acrylic plates to provide the revolutions per minute (RPM) of the propeller with the accuracy of $\approx 0.5\%$. The RPM measurements are synced with other measurements via the data acquisition system (DAQ) at the rate of 1 kHz or higher. Each measurement point represents the data averaged over 2 s in steady states.

B. Experiments

1) Propeller With a 23-mm Radius: For the first motor–propeller combination, 7×16-mm coreless dc motors and propellers with a 23-mm radius ($R = 23$ mm) commercially available as parts for Crazyflie 2.0 were chosen for the experiments. DC signals between 2.5 and 4.0 V generated by the DAQ were used as an input reference for high-current amplifiers (OPA548T, Texas Instruments) in the voltage follower configuration for directly driving the dc motors. Current sensors (INA169, Texas Instruments) were incorporated to measure the current in the range of 0–5 A with the errors of 2%. The voltage across each motor was also monitored through the DAQ. In the experiments, each motor consumed the maximum of ≈ 1.1 A.

For 23-mm propellers, we first tested a single propeller with the propeller axis aligned with the $\hat{z}$-axis of the force/torque sensor. This enabled simultaneous measurements of force and torque. In steady states, the force represents the axial thrust generated by the propeller and the axial torque is the aerodynamic drag.

To study the multirotor interaction, four propellers were mounted in a symmetric "+" configuration using a 3-D printed frame. We experimented with different distances between opposite propellers ($L = 78, 85, 92,$ and 106 mm). In this setting, both clockwise and counter-clockwise rotating propellers were

used to imitate a real quadrotor. As a consequence, only the force (thrust) measurements are available.

For each configuration, the propeller-to-ceiling distance was varied from 1 to 100 mm, resulting in 68 different distances. At each distance, 16 driving voltages were commanded. This resulted in approximately 1000 measurements for each configuration. In the presentation of the results, all measurements corresponding to multirotor configurations are normalized to represent the values per one propeller.

2) Propeller With a 50-mm Radius: To show that the proposed model applies generally to not only one propeller size, we employed a 50-mm radius ($R = 50$ mm) carbon fiber propeller paired with a brushless dc motor (MultiStar Viking 2206–2600 kv) for a single propeller experiment. Here, a PWM signal directly generated by the DAQ was used as command signals for an ESC (Plush 25 A, Turnigy) to produce three-phase signals required by the brushless motor. A 12-V power supply unit (DS550-3, Astec) was used to provide the power to the motor via the ESC. The supplied voltage across the ESC was monitored through the DAQ, whereas the consumed current was also measured using a current sensor (GHS 10-SME, LEM USA). In the experiments, the averaged current varied from 1.5 to 10.2 A, while the voltage remained approximately constant at $\approx 12.2 - 12.3$ V.

With this propeller, experiments with a single propeller were performed at 68 propeller-to-ceiling distances from 1 to 105 mm. At each distance, 16 values of PWM signals were used. The measurements of RPM, voltage, current, force, and torque were recorded. In total, over 1000 data points were taken.

VI. EXPERIMENTAL RESULTS AND ANALYSIS

A. Measurement Results

Fig. 3(a) shows the measurements of thrust and angular velocity of a single 23-mm propeller versus the input power into the system (P_i) at some representative distances from the ceiling (other measurements are omitted for clarity). Overall, as the driving voltage increases, the current and, therefore, power, rise as expected. This results in higher thrust forces and angular velocities. Without the ceiling, the maximum thrust value is 0.18 N. This value increases dramatically with the ceiling, reaching 0.45 N (2.5 times of 0.18 N) when the ceiling is 1.0 mm from the propeller ($D = 1.0$ mm, $\delta = 23.0$) while the input power remains approximately unchanged. In terms of the rotational rate, relatively little changes are observed when the ceiling is introduced. The angular velocity is primarily dependent on the driving voltage rather than the distance to the ceiling. Measurements corresponding to multirotor configurations, which are not shown, are found to feature similar characteristics.

In case of the 50-mm propeller, similar trends are seen in Fig. 3(c). The effects of the ceiling are visible, but not as pronounced. For example, the maximum thrust force increases from 3.7 N without the ceiling to 5.6 N (1.5 times of 3.7 N) when the ceiling is 2 mm away ($D = 2$ mm, $\delta = 25.0$). Similarly, the presence of the ceiling only slightly affects the angular velocity.
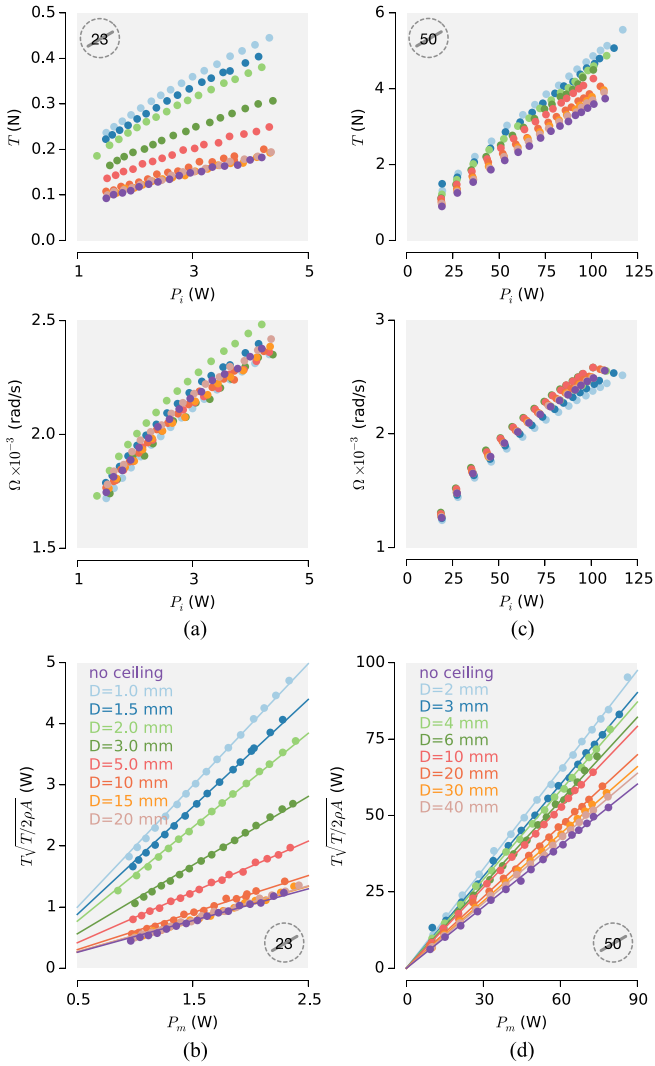
Fig. 3.   Measurements of thrust and rotational rates against input power and mechanical power for (a) 23-mm propeller. (b) 50-mm propeller, both in a single propeller setting.

B. Calculation of Mechanical Power

To determine the ceiling coefficients, it is required to evaluate the mechanical power outputted by the motors. For a single 23-mm propeller with a coreless motor, the mechanical power can be deduced as $P_m = \tau\Omega$ from the measurements of torque and angular velocity. To determine the mechanical power for multirotor configurations, where the propeller torques cancel out, the first-order motor model $V = IR_i + k\Omega$ or $P_i = IV = I^2R_i + P_m$ as outlined in Section III-C is considered. With the knowledge of $P_m = \tau\Omega$ from a single propeller case (where the measurements of τ is available) and measurements of I and V, we solve for R_i from the equation $P_i = I^2R_i + P_m$ using the least-squares method. Assuming this R_i is identical for all motors, the least-squares method is applied to determine k from $V = IR_i + k\Omega$ based on the measurements of V, I, and Ω. The resultant R_i and k are found to be 1.58 Ω and 1.1 mV·s·rad^{-1}. The mechanical power is then given as $P_m = Ik\Omega$.

In case of the 50-mm propeller, only experiments with a single propeller were performed. The mechanical power is, therefore, readily available as $P_m = \tau\Omega$. The measurements of V and I provide the input power only for reference and comparison.

C. Ceiling Coefficients

1) Ceiling Coefficients From the Experiments: From the calculated mechanical power, we plot P_m against $T\sqrt{T/2\rho A}$ as suggested by (7) and (11) using $\rho = 1.2$ kg·m^{-3}. For each particular distance from the ceiling, the data points from different commanded signals amount to the best fit line, of which the slope corresponds to the inverse of the ceiling coefficient times the figure of merit ($P_m = \frac{1}{\eta\gamma}T\sqrt{T/2\rho A}$). This allows η and γ to be empirically deduced from the power and thrust measurements. Examples of the plots are given in Fig. 3(b) and (d) for single propeller tests for both 23-mm and 50-mm propellers. It can be seen that the relationship between P_m and $T\sqrt{T/2\rho A}$ is linear as anticipated. The corresponding figures of merit for the 23-mm and 50-mm propellers are $\eta = 0.50$ and 0.68, respectively. The values imply that the smaller propeller is aerodynamically less efficient as expected [29], [30]. Moreover, the ceiling coefficients deduced from the gradients increase as the distance to the ceiling reduces. The trend is visibly more prominent for the 23-mm propeller. The plots for other propeller configurations are omitted for brevity.

The ceiling coefficients found from the experimental data [the gradients of fitted lines in Fig. 3(b) and (d)] for all propeller configurations are plotted against δ as points in Fig. 4(a)–(f). It can be seen that the presence of the ceiling boosts the values of γ significantly. For a single 23-mm propeller, the ceiling coefficients increase from unity to $\gamma \approx 4$, when $\delta = 23$ or $D = 1.0$ mm. The implies that, at 1.0 mm from the ceiling, the thrust is amplified by a factor of $4^{2/3}$ or 2.5 times for the same power consumption, consistent with the observations in Fig. 3. The ceiling effects, however, appear less prominent for propellers in quadrotor configurations. The coefficients for the multirotor cases maximize around $\approx 3 - 3.5$ and are qualitatively similar for all L's. The effects of the ceiling are also evident for a 50-mm propeller, nevertheless, the increase in thrust is notably smaller than that of the 23-mm propeller. At $\delta = 25$ or $D = 2$ mm, γ is approximately 1.6, suggesting a 37% improvement in thrust given the same power consumption. Furthermore, we observe an anomalous dip in the values of γ near $\delta \approx 7.1$. In fact, similar features are also perceived with 23-mm propellers near $\delta \approx 9.2$, to a smaller extent. We believe this is caused by unmodeled power losses as discussed further in Section VI-D2 and the supplemental materials.

2) Proposed Models of the Ceiling Coefficients: Next, the empirically computed ceiling coefficients are taken to evaluate the best-fitted coefficients (α_0 and α_1) of the proposed model as described in (10). First, α_1 is first assumed to be zero. In other words, the wake recirculation is neglected.

This reduced model is similar to our preliminary findings presented in [27]. The reduced model is found to be sufficiently accurate to describe the observed ceiling effects for a single 23-mm propeller when $\delta < 20$. The prediction of the ceiling
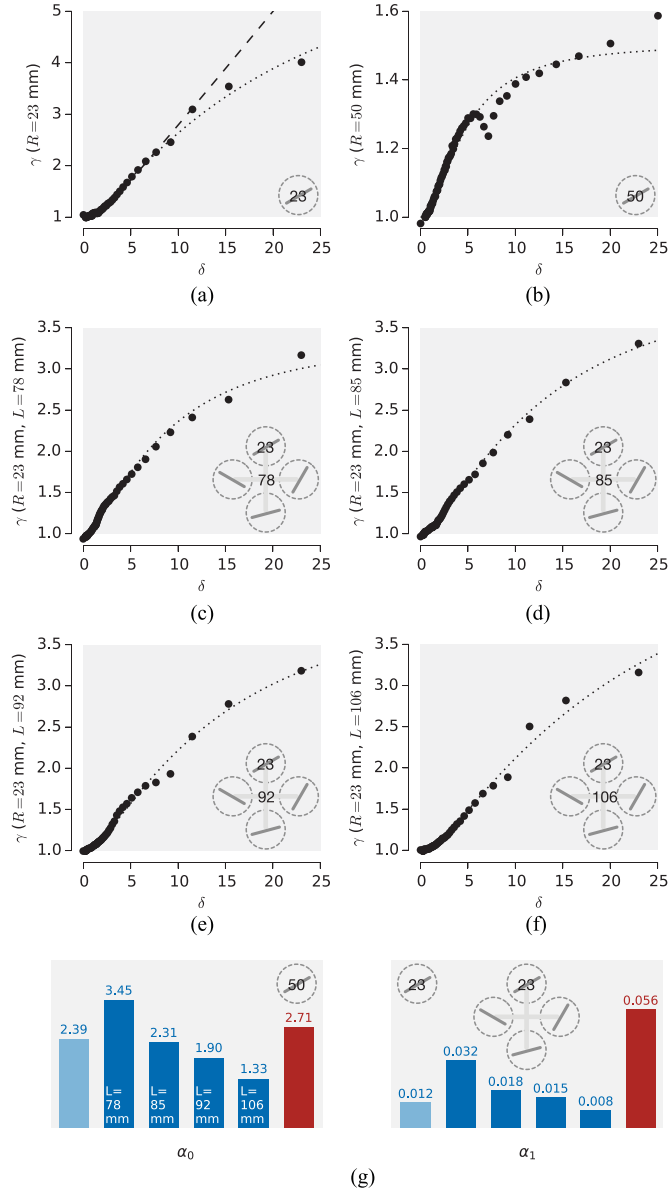
Fig. 4. Empirical ceiling coefficients (points) compared to the proposed model (dashed line for the reduced model and dotted lines for the full model). (a) Single 23-mm propeller. (b) Single 50-mm propeller. (c)–(f) Four 23-mm propellers arranged in a quadrotor configuration with $L = 78, 85, 92,$ and 105 mm. (g) Fitted model coefficients for six tested propeller configurations.

coefficients compared to the empirical results are shown as the dashed line and points in Fig. 4(a) with $\alpha_0 = 1.60$. Nevertheless, we find that the reduced model overestimates the ceiling coefficients at higher δ or when it is applied to other propeller settings. The results indicate that the flow recirculation, which captures the partial loss of terminal flow momentum, must be taken into account.

The dotted lines in Fig. 4(a)–(f) represent the fitted models with recirculation based on (10) for both propeller sizes at different configurations. The corresponding numerical coefficients accounting for the asymmetric flow and recirculation (α_0 and α_1) for all configurations are shown in Fig. 4(g). Apart from the

unexpected dip in γ at $\delta \approx 7.1$ and 9.2 mentioned earlier, the proposed models accurately describe the experimental results in both single and multirotor settings for 23-mm propellers, whereas in the case of the larger propeller, the model slightly underpredicts the ceiling coefficient when the propeller is extremely close to the ceiling ($\delta = 24$, $D = 2$ mm).

A closer inspection of Fig. 4(g) reveals that, the asymmetric flow parameters (α_0) are all above unity, suggesting some degree of asymmetry in all settings. In particular, it can be seen that, for quadrotor-like configurations, the value of α_0 grows as the distance between the propeller shrinks, consistent with the assumption of flow interaction. Simultaneously, we observe an increase in the recirculation factor (α_1) as L reduces. The observations are reasonable as the presence of other rotors in vicinity would introduce recirculation and enhance the asymmetrical flow pattern as we speculated earlier. The competing effects of α_0 and α_1 make the resultant ceiling coefficients for all multirotor configurations qualitatively similar as seen in Fig. 4(c)–(f).

Compared to the small propellers, the fitted coefficients for the 50-mm propeller signify markedly higher flow recirculation [see Fig. 4(g)]. Based on this finding, recirculation is a major factor that demotes the ceiling effects for the large propeller. It is also likely that, at extremely small gap sizes ($\delta > 20$), the presence of the ceiling starts to disrupt the recirculation, resulting in larger ceiling coefficients than predicted by the fitted model, explaining the observation in Fig. 4(b).

D. Thrust and Torque Coefficients For Flight

1) Thrust and Torque Coefficients From the Experiments: The measurements of thrust, torque, and angular velocity enable the calculation of thrust and torque coefficients of the propellers as $c_T := T/\Omega^2$ and $c_\tau := \tau/\Omega^2$. Without a ceiling, these coefficients are constant and only dependent on the propeller profiles. Without precise knowledge of the blade profile, c_T and c_τ are typically experimentally determined for flight control purposes. With a ceiling in proximity, the BEMT analysis suggests that these coefficients also depend on δ and η as given by (14) and (15), respectively.

Focusing on single propeller cases, of which the torque measurements are available, T and τ are plotted against Ω^2 to compute c_T and c_τ corresponding to different ceiling distances from the gradients. Example data from some representative distances are illustrated in Fig. 5. The linear relationships between T and τ with respect to Ω^2 qualitatively verify the validity of (14) and (15), which can be interpreted as, there exist constant values of c_T and c_τ for a fixed propeller-to-ceiling distance.

2) Fitted Models For Thrust and Torque Coefficients: The analytical expressions of c_T and c_τ are functions of δ and the dimensionless parameters: $c_0, c_1,$ and c_2, according to (14) and (15). Since it is not practical to calculate these parameters for propellers with sophisticated profiles, the values of $c_0, c_1,$ and c_2, that best fit our experimental data from Fig. 5 are numerically determined for both c_T and c_τ. The parameters for both propellers are listed in Table I. The thrust and torque coefficients
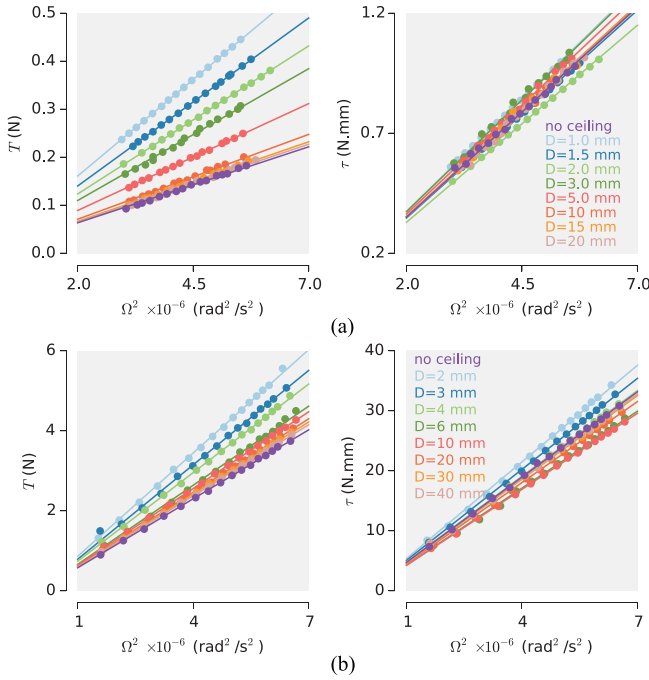
Fig. 5. Raw measurements of thrust and torque plotted with respect to the squared rotational rates at different propeller-to-ceiling distances. (a) Measurements from a single 23-mm propeller. (b) Measurements from a single 50-mm propeller.
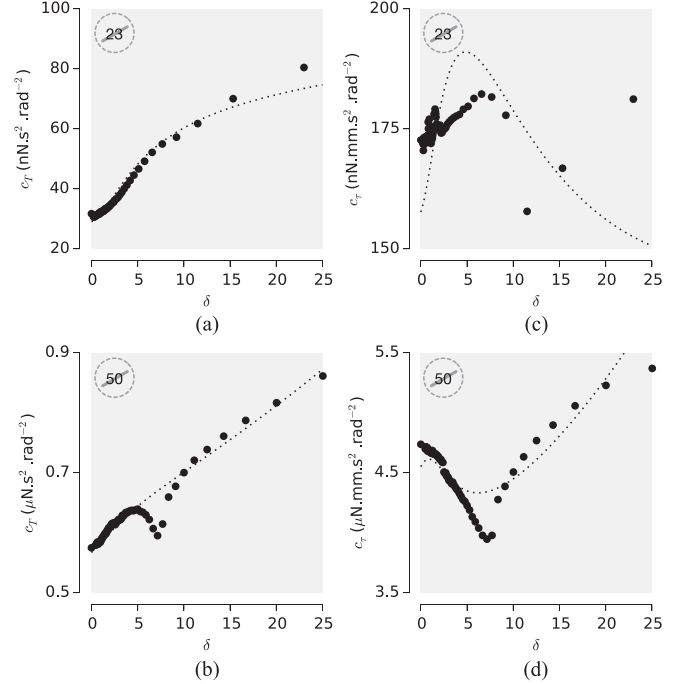

Fig. 6. Flight coefficients as calculated from the benchtop experiments (points) and from the fitted models (dotted lines). (a) Thrust coefficient of a 23-mm propeller. (b) Torque coefficient of a 23-mm propeller. (c) Thrust coefficient of a 50-mm propeller. (d) Torque coefficient of a 50-mm propeller.

TABLE I
PROPELLER COEFFICIENTS

Propellers	c_0	c_1	c_2	$c_T\|_{\delta=0}$ (Ns^{2}rad^{-2})	$c_\tau\|_{\delta=0}$ (Nms^{2}rad^{-2})
23 mm	0.154	0.846	0.022	29.0×10^{-9}	158×10^{-12}
50 mm	0.058	0.095	0.011	0.57×10^{-6}	4.55×10^{-9}

corresponding to these parameters are plotted (dotted lines) alongside the empirical results (points) in Fig. 6.

Overall, the fitted models agree with the experimental data for all δ's. In the case of the 23-mm propeller, the model for the thrust coefficient correctly predicts the magnification of more than 2.5 times when the ceiling is 1.5 mm ($\delta \approx 15$) away from the propeller, with a slight deviation at $D = 1.0$ mm ($\delta = 23$). The model appears similarly accurate in estimating the thrust coefficients for the 50-mm propeller, with the exception being when δ is near 9.2, where the irregular drop in the values of γ is observed [refer to Fig. 4(b)].

While the anomaly cannot be directly explained by the proposed models, during the experiments, the 50-mm propeller generated abnormally loud noises when δ is near 9.2. As suggested by the analysis of mechanical resonance given in the supplemental materials, it is highly possible that in this region, the propeller rotated at frequencies near the standing wave frequency of the experimental setup. The condition may have affected the wake, resulting in the oscillation that renders MT inaccurate at predicting the flow dynamics.

For torque coefficients, at the first glance, the discrepancy between the predictions of c_τ and the data seems substantial,

particularly for the 23-mm propeller. One possible reason is the calculation of c_τ assumes the figure of merit remains constant. This may not be entirely accurate as the ceiling might have influenced the rotational component of the wake. Despite that, a closer inspection reveals that the model is sufficiently accurate as it predicts minor changes in c_τ, on the order of 20% compared to the no ceiling case. Over the range of $\delta < 20$, the differences between the empirical c_τ and predicted c_τ are less than $\approx 10\%$. For the small propeller, the model correctly predicts the existence of a peak in c_τ (though the peak location is slightly misaligned from the experimental results). In total, we see that the proposed model is able to describe two qualitatively distinct c_τ profiles obtained from different propeller sizes.

The findings on c_T and c_τ here are consistent with the initial measurements from Fig. 3. The fact that the presence of a ceiling only marginally affects c_τ means that it only has minor influences on the power. Consequently, we observe little changes in the rotational rates given the input power. In the meantime, the dramatic change in c_T is consistent with the marked changes in resultant thrust at different ceiling distances for the same input power.

VII. DISCUSSION AND FUTURE WORK

With foreseeable potential as an energy conserving strategy for small flying robots, this paper studied the effects of ceiling in proximity to a small spinning propeller. Based on a few simplifying assumptions, MT and the BEM were employed to derive analytical models that describe the thrust, power, and

rotational velocity of a spinning propeller. The formulations were extended to take into account the presence of nearby propellers to imitate the propellers in multirotor vehicles. This was achieved by consideration of wake recirculation and asymmetrical flow pattern. Benchtop experiments involving propellers with 23-mm and 50-mm radii in single and multirotor settings were performed and the results obtained are consistent with our model predictions.

As suggested by the model, we found that the ceiling can radically affect the power consumption and thrust generated by propellers. For small propellers arranged in a quadrotor-like configuration, we observe a reduction in mechanical power by a factor of three or more. Whereas for a 50-mm propeller, the change in power efficiency is lower, the improvement of approximately 50% is still substantial. While the current study is still limited to flat, rigid, and horizontal ceilings, we believe our promising outcomes here offer an opportunity to alleviate the issue of diminished flight endurance of small rotorcraft.

It is, however, challenging to realize a flight with surface locomotion in practice. The strategy necessitates the design of a lightweight mechanism that impedes the robot from directly colliding with the ceiling, absorbs the kinetic energy from impact to prevent bouncing, and maintains a suitable propeller-to-ceiling distance. In terms of flight control, a controller must be devised to deal with the ceiling approach (which could be different from a regular landing maneuver). Not only must the controller be able to regulate the thrust appropriately once the robot is in contact with the ceiling, but it also has to retain the attitude and spatial stability with the presence of the normal force from the ceiling. For these reasons, the realization of surface flight is beyond the scope of this work. Still, an extended analysis on the power saving potential and a preliminary design of a lightweight mechanism that would allow the robot to safely approach the ceiling for the proposed surface locomotion are provided below.

A. Power Saving Potential

The analysis of the ceiling effects provided in this work relates the thrust force to the aerodynamic power. Together with the assumption that the aerodynamic power is proportional to the mechanical power ($P_m = \eta P_a$), it has been shown that the reduction in mechanical power is given by the ceiling coefficient. In an actual robot, the input power provided to the motor–propeller pair, however, is different from the mechanical power as it includes frictional and dissipative losses. In order to estimate the realistic power saving from the ceiling effects, the analysis is expanded to include the input power for the case of 23-mm propellers in a quadrotor configuration with the motor-to-motor distance $L = 92$ mm—identical to the configuration of a commercially available Crazyflie 2.0 nanoquadrotor. The estimates of input power, therefore, provide more realistic numbers for calculating how much power saving could be achieved in practice.

The input power analysis begins by revisiting the first-order brushed motor model: $V_i = IR_i + k\Omega$, the definitions of P_m as $P_m = \tau\Omega = Ik\Omega$, and the torque coefficient: $c_\tau = \tau/\Omega^2$. From earlier findings in Fig. 6(c), it is reasonable to assume that c_τ is
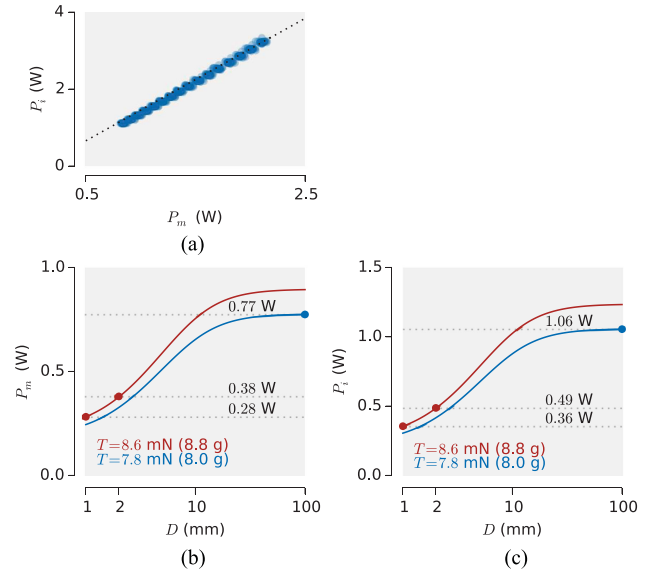

Fig. 7. (a) Measured mechanical power and input power (blue points) and the model prediction (dotted line). (b) The plot of the mechanical power required to sustain 7.8 mN (blue) and 8.6 mN (red) thrust at different ceiling distances. (c) The plot of the input power required to sustain 7.8 mN (blue) and 8.6 mN (red) thrust at different ceiling distances.

approximately constant, regardless of the distance to the ceiling. In such circumstances, we modify the motor model to represent the input and mechanical power as

$$P_i = c_\tau^{2/3} k^{-2} R_i \cdot P_m^{4/3} + P_m. \tag{16}$$

Using the same identified parameters from the experiments, $R = 1.58\ \Omega$, $k = 1.1$ mV·s·rad^{-1}, and assuming a constant c_τ of 175 nN·mm·s^2·rad^{-2}, the predicted relationship between P_m and P_i for the system is shown in Fig. 7(a). The plot verifies that (16) matches the experimental data with reasonable accuracy.

According to the datasheet, the original Crazyflie 2.0 weighs 28 g. For practical flight with some safety margin, each propeller is required to generate approximately an equivalent of 8 g of thrust force (or $T = 7.8$ mN) for the robot to hover. The required mechanical power for the respective thrust is computed from (7). With the model of ceiling coefficients for this particular robot configuration [see, Fig. 4(e)], the mechanical power at different ceiling-to-propeller distances needed to generate $T = 7.8$ mN are shown in Fig. 7(b). Furthermore, the mechanical power is translated into the input power and shown in Fig. 7(c). The plots suggest that the mechanical and input powers required for each propeller in a near hovering condition for the robot are approximately 0.77 and 1.06 W.

To leverage the ceiling effects for surface locomotion, we believe it is necessary for the robot to generate the total thrust with a greater magnitude than its weight such that there remains some normal force against the ceiling. This normal force ensures contact between the robot and the ceiling, and, therefore, maintains a constant separation. On the assumption that the robot requires an additional of 10% on thrust ($T = 8.6$ mN or 8.8 g), the corresponding powers for different ceiling distances
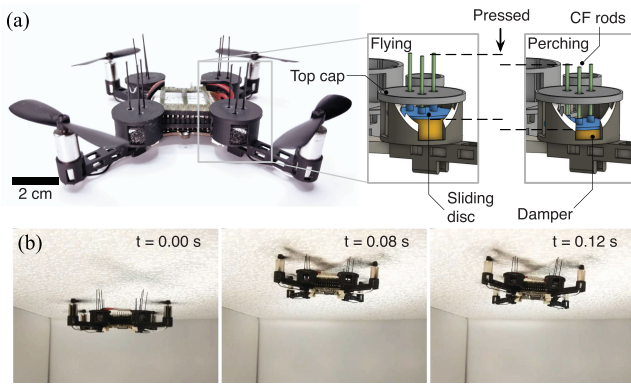
Fig. 8. (a) Proof-of-concept prototype. The modified airframe features a damping component that prevents the propellers from crashing directly into a ceiling using carbon fiber rods. The kinetic energy is dissipated with the incorporation of viscoelastic material. (b) Image sequence showing the transition from aerial to surface locomotion.

are illustrated in Fig. 7(b) and (c). The calculation shows that the required mechanical and input powers for each propeller are 0.38 and 0.49 W, when $D = 2.0$ mm or 0.28 and 0.36 W, when $D = 1.0$ mm. From these estimates, the use of ceilings for surface locomotion has the potential to reduce power consumption of the robot by a factor of $2-3$. While these numbers only account for the actuation and do not reflect the power expended in the controller or communication, the high energetic requirement of flight at small scales means the actuation power constitutes a major proportion of the total power.

B. Conceptual Perching Demonstration

As stated, to demonstrate a ceiling locomotion of a small flying robot, it necessitates a revision in mechanical designs of the robot and a modification in the flight controller. Here, we present a preliminary design of the mechanism that 1) keeps the propeller-to-ceiling distance constant during perching; 2) absorbs kinetic energy upon impact; and 3) is lightweight.

Using the Crazyflie 2.0 as a platform, the airframe is redesigned with a damping element situated on each arm as shown in Fig. 8(a). The damping module is a hollow plastic cylinder, with a snap-on top cap (in false-color green). The damping mechanism consists of a viscoelastic element (false-color yellow, damper) sitting at the bottom, followed by a sliding disc (false-color blue) with attached carbon fiber (CF) rods (false-color purple, CF). The CF rods act as a structure preventing the propellers from directly colliding with the ceiling. Upon an impact with the ceiling, the CF rods and the base disc recede down along the guided path and compress the viscoelastic component. The dissipated energy reduces the bounces observed in flight tests.

This initial design can be further tailored in future work. Currently, with the added structure, the weight of the robot modestly increases from 28 to 30 g. As a proof-of-concept device, we show that this simple mechanism is sufficient for a robot to perch on an overhang in a human-operated flight test as presented in Fig. 8(b).

REFERENCES

[1] S. Thurrowgood, R. J. Moore, D. Soccol, M. Knight, and M. V. Srinivasan,, "A biologically inspired, vision-based guidance system for automatic landing of a fixed-wing aircraft," *J. Field Robot.*, vol. 31, no. 4, pp. 699–727, 2014.

[2] P. Oettershagen *et al.*, "Perpetual flight with a small solar-powered UAV: Flight results, performance analysis and model validation," in *Proc. IEEE Aerosp. Conf( ).*, 2016, Paper 7500855.

[3] Y. Mulgaonkar, A. Makineni, L. Guerrero-Bonilla, and V. Kumar, "Robust aerial robot swarms without collision avoidance," *IEEE Robot. Automat. Lett.*, vol. 3, no. 1, pp. 596–603, Jan. 2018.

[4] G. Vásárhelyi, C. Virágh, G. Somorjai, T. Nepusz, A. E. Eiben, and T. Vicsek, "Optimized flocking of autonomous drones in confined environments," *Sci. Robot.*, vol. 3, no. 20, 2018, Art. no. eaat3536.

[5] P. Chirarattananon, K. Y. Ma, and R. J. Wood, "Perching with a robotic insect using adaptive tracking control and iterative learning control," *Int. J. Robot. Res.*, vol. 35, no. 10, pp. 1185–1206, 2016.

[6] Y. Chen *et al.*, "A biologically inspired, flapping-wing, hybrid aerial-aquatic microrobot," *Sci. Robot.*, vol. 2, no. 11, 2017, Art. no. eaao5619.

[7] D. Floreano and R. J. Wood, "Science, technology and the future of small autonomous drones," *Nature*, vol. 521, no. 7553, pp. 460–466, 2015.

[8] K. Karydis and V. Kumar, "Energetics in robotic flight at small scales," *Interface focus*, vol. 7, no. 1, 2017, Art. no. 20160088.

[9] P.-E. J. Duhamel, N. O. Pérez-Arancibia, G. L. Barrows, and R. J. Wood, "Biologically inspired optical-flow sensing for altitude control of flapping-wing microrobots," *IEEE/ASME Trans. Mechatronics*, vol. 18, no. 2, pp. 556–568, Apr. 2013.

[10] P. Chirarattananon, "A direct optic flow-based strategy for inverse flight altitude estimation with monocular vision and IMU measurements," *Bioinspiration Biomimetics*, vol. 13, no. 3, 2018, Art. no. 036004.

[11] T. Oktay and C. Sultan, "Comfortable helicopter flight via passive/active morphing," *IEEE Trans. Aerosp. Electron. Syst.*, vol. 51, no. 4, pp. 2876–2886, Oct. 2015.

[12] F. Morbidi, R. Cano, and D. Lara, "Minimum-energy path generation for a quadrotor UAV," in *Proc. IEEE Int. Conf. Robot. Autom.*, 2016, pp. 1492–1498.

[13] P. Gnemmi *et al.*, "Conception and manufacturing of a projectile-drone hybrid system," *IEEE/ASME Trans. Mechatronics*, vol. 22, no. 2, pp. 940–951, Apr. 2017.

[14] L. Daler, S. Mintchev, C. Stefanini, and D. Floreano, "A bioinspired multi-modal flying and walking robot," *Bioinspiration Biomimetics*, vol. 10, no. 1, 2015, Art. no. 016005.

[15] H. Alzu'bi, I. Mansour, and O. Rawashdeh, "Loon copter: Implementation of a hybrid unmanned aquatic–aerial quadcopter with active buoyancy control," *J. Field Robot.*, vol. 35, no. 3, pp. 764–778, 2018.

[16] R. Siddall and M. Kovac, "Fast aquatic escape with a jet thruster," *IEEE/ASME Trans. Mechatronics*, vol. 22, no. 1, pp. 217–226, Feb. 2017.

[17] W. R. Roderick, M. R. Cutkosky, and D. Lentink, "Touchdown to take-off: At the interface of flight and surface locomotion," *Interface Focus*, vol. 7, no. 1, 2017, Art. no. 20160094.

[18] A. Kalantari, K. Mahajan, D. Ruffatto, and M. Spenko, "Autonomous perching and take-off on vertical walls for a quadrotor micro air vehicle," in *Proc. IEEE Int. Conf. Robot. Automat.*, 2015, pp. 4669–4674.

[19] M. Graule *et al.*, "Perching and takeoff of a robotic insect on overhangs using switchable electrostatic adhesion," *Sci.*, vol. 352, no. 6288, pp. 978–982, 2016.

[20] M. T. Pope *et al.*, "A multimodal robot for perching and climbing on vertical outdoor surfaces," *IEEE Trans. Robot.*, vol. 33, no. 1, pp. 38–48, Feb. 2017.

[21] K. Hang *et al.*, "Perching and resting-a paradigm for UAV maneuvering with modularized landing gears," *Sci. Robot.*, vol. 4, no. 28, 2019, Art. no. eaau6637.

[22] A. Betz, "The ground effect on lifting propellers," *Zeitschrift fur angewandte Mathematik und Mechanik*, vol. 17, no. 2, pp. 68–72, 1937.

[23] D. A. Griffiths, S. Ananthan, and J. G. Leishman, "Predictions of rotor performance in ground effect using a free-vortex wake model," *J. Amer. Helicopter Soc.*, vol. 50, no. 4, pp. 302–314, 2005.

[24] G. J. Leishman, *Principles of Helicopter Aerodynamics with CD Extra*. Cambridge, U.K.: Cambridge Univ. Press, 2006.

[25] E. Davis and P. E. Pounds, "Passive position control of a quadrotor with ground effect interaction," *IEEE Robot. Automat. Lett.*, vol. 1, no. 1, pp. 539–545, Jan. 2016.

[26] C. Powers, D. Mellinger, A. Kushleyev, B. Kothmann, and V. Kumar, "Influence of aerodynamics and proximity effects in quadrotor flight," in *Proc. 13th Int. Symp. Exp. Robot.*, 2013, pp. 289–302.

[27] Y. H. Hsiao and P. Chirarattananon, "Ceiling effects for surface locomotion of small rotorcraft," in *Proc. IEEE/RSJ Int. Conf. Intell. Robots Syst.*, 2018 pp. 6214–6219.

[28] J. M. Seddon and S. Newman, *Basic Helicopter Aerodynamics*, vol. 40. Hoboken, NJ, USA: Wiley, 2011.

[29] M. Bangura, M. Melega, R. R. Naldi, and R. Mahony, "Aerodynamics of rotor blades for quadrotors," 2016, pp. 11773–11780, *arXiv:1601.00733*.

[30] M. Bangura and R. Mahony, "Thrust control for multirotor aerial vehicles," *IEEE Trans. Robot.*, vol. 33, no. 2, pp. 390–405, Apr. 2017.

[31] E. Branlard, *Wind Turbine Aerodynamics and Vorticity-Based Methods.* New York, NY, USA: Springer, 2017.

[32] J. S. Light, "Tip vortex geometry of a hovering helicopter rotor in ground effect," *J. Amer. Helicopter Soc.*, vol. 38, no. 2, pp. 34–42, 1993.

[33] N. D. Nathan," PhD dissertation, Univ. Glasgow, Glasgow, Scotland, 2010.

Pakpong Chirarattananon (S'12–M'15) received the B.A. degree in natural sciences from the University of Cambridge, Cambridge, U.K., in 2009, and the Ph.D. degree in engineering sciences from Harvard University, Cambridge, MA, USA, in 2014.

He is currently an Assistant Professor with the Department of Biomedical Engineering, City University of Hong Kong, Hong Kong SAR, China. His research interests include bio-inspired robots, micro air vehicles, and applications of control in robotic systems.

Yi Hsuan Hsiao is currently working toward the bachelor's degree in mechanical engineering with a minor in computing at the City University of Hong Kong, Hong Kong SAR, China.

His research interests include micro air vehicles, mechanical design of flapping-wing robots, and rotorcraft surface locomotion.